

X-ray free electron laser heating of water and gold at high static pressure

Rachel J. Husband¹✉, R. Stewart McWilliams², Edward J. Pace², Amy L. Coleman³, Huijeong Hwang^{4,8}, Jinhyuk Choi⁴, Taehyun Kim⁴, Gil Chan Hwang⁴, Orianna B. Ball², Sae Hwan Chun⁵, Daewoong Nam⁵, Sangsoo Kim⁵, Hyunchoe Cynn³, Vitali B. Prakapenka⁶, Sang-Heon Shim⁷, Sven Toilekis¹, Malcolm I. McMahon², Yongjae Lee⁴ & Hanns-Peter Liermann¹

Probing of reactive materials such as H₂O ices and fluids at the high pressures and temperatures of planetary interiors is limited by unwanted chemical reactions and confinement failure. Faster experiments can mitigate such issues, but the common approach of adiabatic compression limits the conditions achieved. This study demonstrates a fast experimental strategy for the creation and probing of selected extreme states using static compression coupled with ultrafast X-ray laser heating. Indirect X-ray heating of H₂O through the use of a gold absorber is evidenced by sample melting inferred from textural changes in the H₂O diffraction lines and inter-dispersion of gold and H₂O melts. Coupled with numerical analysis of femtosecond energy absorption, thermal equilibration, and heat transfer, all evidence indicates that temperatures in excess of an electron volt have been reached in the H₂O at high pressure. Even after repeated heating, samples stayed chemically unchanged from the starting material.

¹Photon Science, DESY, Notkestrasse 85, Hamburg, Germany. ²SUPA, School of Physics and Astronomy & Centre for Science at Extreme Conditions, The University of Edinburgh, Edinburgh, UK. ³Lawrence Livermore National Laboratory, Livermore, CA, USA. ⁴Department of Earth System Sciences, Yonsei University, Seoul, Republic of Korea. ⁵Pohang Accelerator Laboratory, Pohang, Gyeongbuk, Republic of Korea. ⁶Center for Advanced Radiation Sources, University of Chicago, Chicago, IL, USA. ⁷School of Earth and Space Exploration, Arizona State University, Tempe, AZ, USA. ⁸Present address: Photon Science, DESY, Notkestrasse 85, Hamburg, Germany. ✉email: rachel.husband@desy.de

Achieving planetary interior conditions in the laboratory is essential for the exploration of planetary structure, evolution, and dynamics, such as the generation of magnetic fields. This is particularly difficult to simulate for planetary bodies comprising light element fluids, including water-rich planets from Super-Earths to Ice Giants, due to the high reactivity and the difficulty of confining samples. Planetary ices such as H₂O, and its mixtures with molecular compounds such as ammonia (NH₃) and methane (CH₄), play a crucial role in both Solar^{1–3} and extrasolar icy planets⁴. As such, the phase transformations and equation of state (EoS) of H₂O ice and its mixtures at high pressures (P) and temperatures (T) have received particular attention^{5–13}. Pure H₂O displays a rich phase diagram, adopting numerous structural polymorphs on compression at ambient T (ice-VI, VII, VII' and X¹⁴) and exhibiting superionic behavior at high P–T conditions, where protons move freely within the oxygen lattice^{15–17}. Structural phase transitions are also observed in the superionic state¹⁸.

A major challenge when studying the phase relations and physical properties of such compounds at simultaneous high P and T relates to their highly reactive nature at these conditions, especially in the molten state. This is particularly challenging for studies performed using diamond-anvil cells (DACs), where reactions between H₂O with the gasket material (typically Re) introduces the possibility of cross-contamination of the sample material. So far, these challenges have limited the conditions accessible to static-compression studies. Similarly, studies using dynamic compression are limited to adiabatic pathways^{16,17} and very short timescales, raising the question of whether the achieved states represent equilibrium conditions¹⁹. Hence, experimental techniques able to achieve selected P–T conditions and timescales are needed. While recent dynamic compression experiments have reported the first clear evidence of the existence of superionic H₂O ice (e.g., Ref. 17), only one diffraction line was used for phase identification in this very challenging experiment. Systematic studies of the entire stability field by employing high-T static-compression techniques are therefore needed, for example, to establish equilibrium phase boundaries.

The use of optical laser heating under static compression in the DAC has long been central in high P–T investigations. Pulsed-laser heating, in which the sample is confined at high P–T conditions for a short period of time, minimizes both the probability of reaction between the sample and its surrounding environment, and sample loss by diffusion, particularly for light element (hydrogen-rich) matter^{20,21}. Yet, optical laser techniques (typically performed in the near-IR) are susceptible to unpredictable or limited heating, controlled by sample optical properties and restrictions on deliverable energy (e.g., through the anvils). This raises the prospect of utilizing pulsed X-ray laser heating from X-ray free-electron lasers (XFELs) as a means to explore more extreme conditions in reactive materials^{22,23}. Unlike conventional high-P synchrotron experiments in which the sample is exposed to $\sim 10^{11}$ photons per second²⁴, each ~ 20 fs (femtosecond) XFEL pulse may contain up to $\sim 10^{11}$ photons^{25,26}. At such high X-ray fluence and short timescale, heating effects become significant, and deliberate application to samples under high P potentially offers an efficient way to heat higher-atomic number (Z) materials, as well as adjacent lower-Z matter through heat conduction²³. In Au, for example, optical heating in the IR is complicated by mirror-like high optical reflectivity of surfaces²⁷, whereas H₂O is transparent, leading to low laser absorption in these substances. Indeed, Au would otherwise be an ideal coupler for laser heating of highly reactive, low-Z matter such as H₂O due to its chemical stability, though whether this remains the case at relevant planetary interior conditions is uncertain. The prospective advantages of an Au coupler may be realized through its

high absorptivity of X-rays, given that, in the case of low-Z materials such as H₂O, the temperature increase induced by direct X-ray heating is too low to achieve conditions of interest due to low X-ray absorption. Meanwhile, XFEL sources enable direct, near-instantaneous probing of sample transformations and properties, e.g., via diffraction²². However, the stability of diamond itself at high X-ray fluences may be of issue²⁸.

Here, we report the results of XFEL irradiation and X-ray diffraction experiments of statically compressed H₂O samples performed at the Pohang Accelerator Laboratory XFEL (PAL-XFEL), South Korea, using an Au foil loaded along with the sample to absorb the XFEL beam. We present clear evidence of indirect X-ray heating of H₂O, based on a combination of X-ray diffraction of temperature-quenched samples and post-experimental analysis of the samples. In all cases, the H₂O samples show no evidence of reactivity, overcoming challenges seen in previous experiments^{7,29}.

Results

XFEL experiment. During the first PAL-XFEL experiment (experiment 1), data were collected on two samples of H₂O and Au using an X-ray energy of 12 keV (samples #1 and #2, see ‘Methods’, Supplementary Methods, and Fig. 1). A schematic of the experimental setup is shown in Fig. 2. These samples were irradiated with single or serial X-ray pulses at 30 Hz at different X-ray fluencies for a range of sample pressures (Fig. 3). First, the X-ray fluence was increased incrementally until diffraction of a sufficient quality was achieved from the Au foil to determine the pressure. Next, the pressure of the sample was increased in steps of 1–10 GPa to the maximum pressure (52 GPa for sample #1 and 62 GPa for sample #2) while collecting diffraction patterns from the Au with an attenuated X-ray fluence for pressure determination. Thereafter, at the highest pressure, the sample was exposed to single XFEL pulses with increasing fluence up to 100%, followed by exposures to multiple pulses at 30 Hz at full fluence. Diffraction data quality was limited by the cBN seats used on the downstream side of the DAC and low X-ray energy; although X-ray-induced changes in the azimuthal intensity of Au diffraction lines due to heating were visible, the quality of the H₂O lines was poor (Supplementary Fig. S1).

Data were therefore collected from two additional samples (samples #3 and #4, see ‘Methods’ and in Supplementary Fig. S2) during a second experimental run (experiment 2) using 14 keV radiation. The sample pressures were adjusted so that sample #3 was in the stability field of ice-VI (2 GPa) and sample #4 was in the stability field of ice-VII (6 GPa). During the XFEL experiment, the Au in each of the samples was exposed to 5 X-ray pulses at 30 Hz and 50% fluence, and the diffraction data collected from samples #3 and #4 are shown in Fig. 4 and Supplementary Fig. S3, respectively. In both cases, significant changes in the azimuthal intensity distribution were observed in both the Au and ice Debye-Scherrer (D-S) rings collected from subsequent X-ray pulses, which can be clearly seen in both the 2D diffraction images and integrated diffraction patterns. The dramatic changes to diffraction patterns confirm that both the Au and the H₂O underwent significant recrystallization following exposures to such high X-ray fluence²², suggesting that both materials were heated (and possibly melted) with direct heating of Au and indirect heating of the adjacent H₂O.

Post-experimental analysis. Photomicrographs of samples #1 and #2 collected after the XFEL experiment are shown in Fig. 1b, d. Sample #1 showed no obvious signs of damage from the XFEL beam exposure. However, when the pressure was released below the melting pressure of H₂O (0.9 GPa³⁰) to recover the sample for

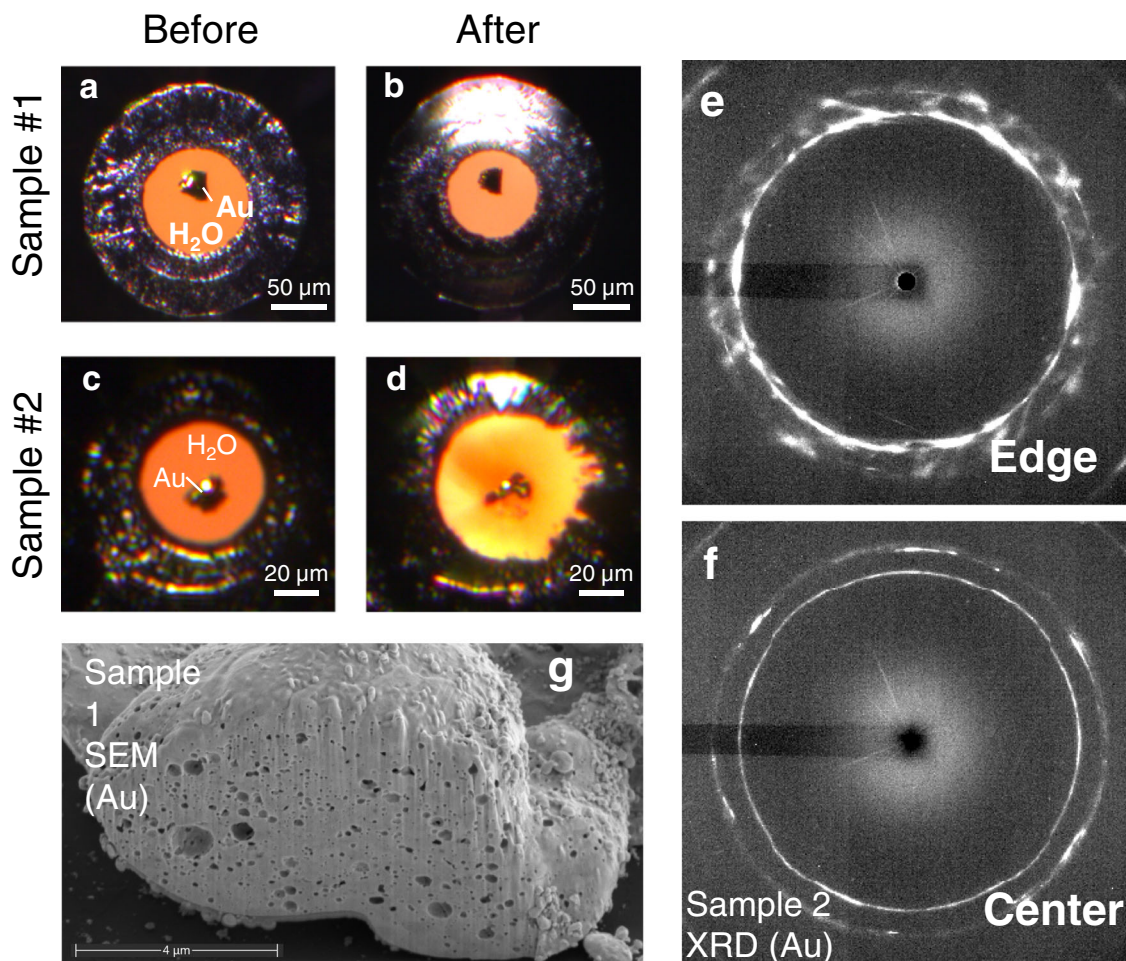


Fig. 1 Sample changes resulting from X-ray heating. **a–d** Photomicrographs of samples #1 and #2 before and after the PAL-XFEL experiment, viewed under transmitted and reflected illumination. **a** Sample #1 before the experiment at 1.7 GPa and **b** after the experiment at 52 GPa, respectively. **c** Sample #2 before the experiment at 2.2 GPa and **d** after the experiment at 62 GPa, respectively. For **(d)** the intensity of transmitted light was varied in order to enhance the color variations in the surrounding H₂O medium. **e, f** Synchrotron X-ray diffraction collected after the experiment from the edge **(e)** and center **(f)** of the Au foil in sample #2. **g** Secondary electron images showing a cross-section through the recovered Au from sample #1.

further analysis, the Au foil partially disintegrated, indicating that the integrity of the Au foil had been significantly altered during the XFEL experiment. Secondary electron images of one of the larger recovered Au pieces (Fig. 1g and Supplementary Fig. S4) revealed a large number of pores in the interior and surface formed due to intermigration of molten H₂O into molten Au during heating. Focused ion beam (FIB) sectioning shows these pores did not only develop near the surface, but also form a 3D network that extends deep into the interior of the Au. The photomicrographs of sample #2 showed even more pronounced changes, with the shape of the Au foil visibly altered in situ, and the orange color of the H₂O medium suggesting that small Au particles had dispersed into the surrounding water³¹ during the heating process. These images clearly evidence melting of the Au foil during the XFEL exposures, and melting of H₂O in contact with the Au, with rapid quenching and freezing of the multiphase fluid mixtures in place.

A synchrotron X-ray diffraction map of these samples (at pressures 52 and 62 GPa for samples #1 and #2, respectively) collected using the sub-micron focusing setup at beamline P02.2 at PETRA III (Supplementary Fig. S5) prior to release showed no evidence of chemical modifications, such as H₂O dissociation resulting from prolonged X-ray irradiation, previously shown to cause a brown discoloration of H₂O samples^{32,33}, or from a

chemical reaction with the gasket or Au coupler such as those observed during optical laser heating^{7,29}. This was confirmed by Raman scattering measurements, in which no sign of O₂ and H₂ vibrons or other chemical reaction products were detected. Although areas of the Au in sample #2 remained at 62 GPa, a pressure gradient of ~30 GPa was present in the H₂O medium. Au could not be detected in the synchrotron micro-diffraction collected from the surrounding orange ice of sample #2 (Supplementary Fig. S5c–f), suggesting that the number of Au particles in these regions is below the detectable limit. Postmortem diffraction from the center of the Au foil showed generally smooth D-S rings from the Au, resulting in sharp diffraction peaks in the integrated diffraction patterns; however, at the edge of the Au foil (e.g., Fig. 1e and Supplementary Fig. S6b) pronounced diffuse scattering was observed in the vicinity of the Au (111) and Au (200) diffraction rings, which resulted in broad tails in the integrated profiles. In addition to a broad diffuse background, distinct non-radial streaks were observed between the (111) and (200) rings (Fig. 1e and Supplementary Fig. S6b). Similar behavior has been observed during fast quenching of molten Fe during high pressure laser-heating experiments in DACs (Z. Konôpková, manuscript in preparation), while strikingly similar diffuse features under pressure in fcc Xe result from stacking disorder attributed to

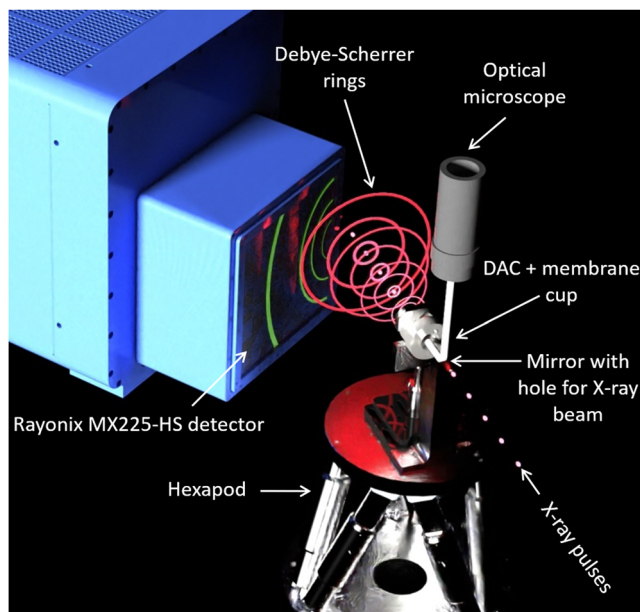


Fig. 2 Schematic showing the experimental setup at the XSS station at PAL-XFEL. X-ray diffraction data were collected on a Rayonix MX225-HS flat panel detector that was horizontally offset to avoid the direct X-ray beam and positioned at an angle of -45° with respect to the incoming beam. The sample was viewed using a camera attached to an optical microscope that was positioned above the sample stage, where optical access to the sample was provided by a mirror with a small hole to allow for transmission of the X-ray beam. The sample holder was placed on a Hexapod stage which was used to position the sample in the beam.

increased stability of the hcp phase³⁴. However, hcp Au has only been observed above 240 GPa at 300 K³⁵ and so may not easily explain the disorder at 62 GPa. Meanwhile, the absence of these features in the bulk Au, despite interpenetration of the melts, rules out chemical contamination. We propose the observed defects arise from fast quenching at the sample edge, producing nanoscopic grains and stacking faults.

Visual observations of samples #1 and #2 showed no visible damage to the diamond anvils induced by X-ray exposure. However, secondary electron images collected from the downstream diamond anvil in sample #1, on which the Au initially rested, showed small pits of $\sim 2\ \mu\text{m}$ in diameter on the diamond surface directly beneath the original position of the Au foil (Supplementary Fig. S7). Similar damage has previously been attributed to diamond melting³⁶, suggesting that the heat transferred from the heated Au foil was sufficient to heat a small region of the diamond surface to above its melting temperature. More significant diamond damage is visible in the photomicrographs of samples #3 and #4 collected after experiment 2 (Supplementary Fig. S2), possibly due to the much smaller beam size used and consequently higher power density of the X-ray beam.

Temperature calculations. While our diagnostic techniques do not yield direct information on the temperature resulting from XFEL exposures, they demonstrate that melting temperatures were exceeded in both Au and H₂O over broad regions of the samples, and for diamond close to the Au coupler. More detailed temperature information is obtained by computing the X-ray coupling with the sample on the basis of measured X-ray fluences, sample geometric properties, and the known physical properties of the samples (Supplementary Methods and Supplementary Table S1)^{23,37}. The calculated temperature–time profile of Au and

H₂O during the exposure of sample #2 to a 48.6 μJ X-ray pulse at 4.7 GPa is shown in Fig. 5. The combination of the large amount of energy deposited in the Au foil and the short timescale of the XFEL pulse (25 fs, shorter than the timescale of the electron-phonon thermalization process) initially brings the irradiated portion of the Au foil to a highly non-equilibrium state where the electrons and ions are at different temperatures, T_e and T_i , respectively, while the H₂O remains cool. At short timescales ($<100\ \text{ps}$), T_e and T_i rapidly evolve toward local thermal equilibrium³⁷ (Supplementary Fig. S8). The bulk of the Au foil expands hydrodynamically following lattice heating, which leads to a rapid partial cooling, followed by heat diffusion from the hot Au to the surrounding cold H₂O²³.

Finite element (FE) models confirm a rapid transfer of heat from the directly heated Au foil into surrounding H₂O. Indeed, later in time, a temperature inversion occurs with the H₂O sample bulk becoming hotter than the Au foil, which cools more rapidly due its proximity to the conductive diamonds (Supplementary Fig. S9d, e). The lifetime and spatial extent of the H₂O hot state depends on pressure, with the heated lifetime about an order of magnitude shorter at 50 GPa compared to 5 GPa, due to increasing thermal transport efficiency between the hot Au and the diamond anvil via the H₂O medium (Supplementary Fig. S10). Absorption of a single incident X-ray pulse at 21% power at 5 GPa, and resultant equilibration processes, result in an initial equilibrium temperature of $\sim 11,000\ \text{K}$ for Au, whereas at 100% power at 50 GPa the predicted peak temperature is close to 50,000 K. As a consequence of the subsequent heat transfer, the FE calculations determined the bulk H₂O should heat up to at least several thousand K (Fig. 6), with the state persisting for about a microsecond (Supplementary Fig. S9); however, a thin layer of H₂O around the Au would heat to significantly higher temperature on shorter timescales (Supplementary Fig. S10), as will the diamond tip.

Discussion

The photomicrographs collected before and after experiment 1 suggest that samples #1 and #2 responded very differently to their respective X-ray exposure histories. While evidence of Au melting and localized H₂O melting was observed in both samples, dispersion of Au particles was only observed for sample #2. Although the image quality of the online optical imaging system at PAL-XFEL was insufficient for us to identify sample changes in situ, we can draw some conclusions based on the differences in the X-ray exposure, pressure, and temperature histories of the two samples. Firstly, their X-ray exposure histories differed at lower pressures; the maximum X-ray fluence during compression of Au in sample #1 did not exceed 5% ($<13\ \mu\text{J}/\text{pulse}$), whereas sample #2 Au was exposed to 21% fluence ($<48\ \mu\text{J}/\text{pulse}$) from $\sim 5\ \text{GPa}$. Secondly, the Au in sample #1 was exposed to significantly higher power (320 $\mu\text{J}/\text{pulse}$) than the Au in sample #2 (60 μJ) at the maximum pressure. These comparisons therefore highly suggest that the large-scale melting of H₂O in sample #2 occurred during irradiation with moderate pulse energies at low pressures, where the melting temperature of H₂O is still relatively low^{6,8,29} (Fig. 6). Both the data and models suggest that at higher pressures, where the Au of sample #1 was exposed to high pulse energies (including multiple pulses at 30 Hz), heating (and melting) of the surrounding medium is suppressed in comparison to lower pressures due to the increased thermal transport efficiency of the H₂O medium.

It can be seen that, particularly early in the simulation, water immediately adjacent to the Au layer is subjected to very high temperatures, well in excess of the melting point, even approaching conditions of a dense plasma^{16,17,38}. A bulk region

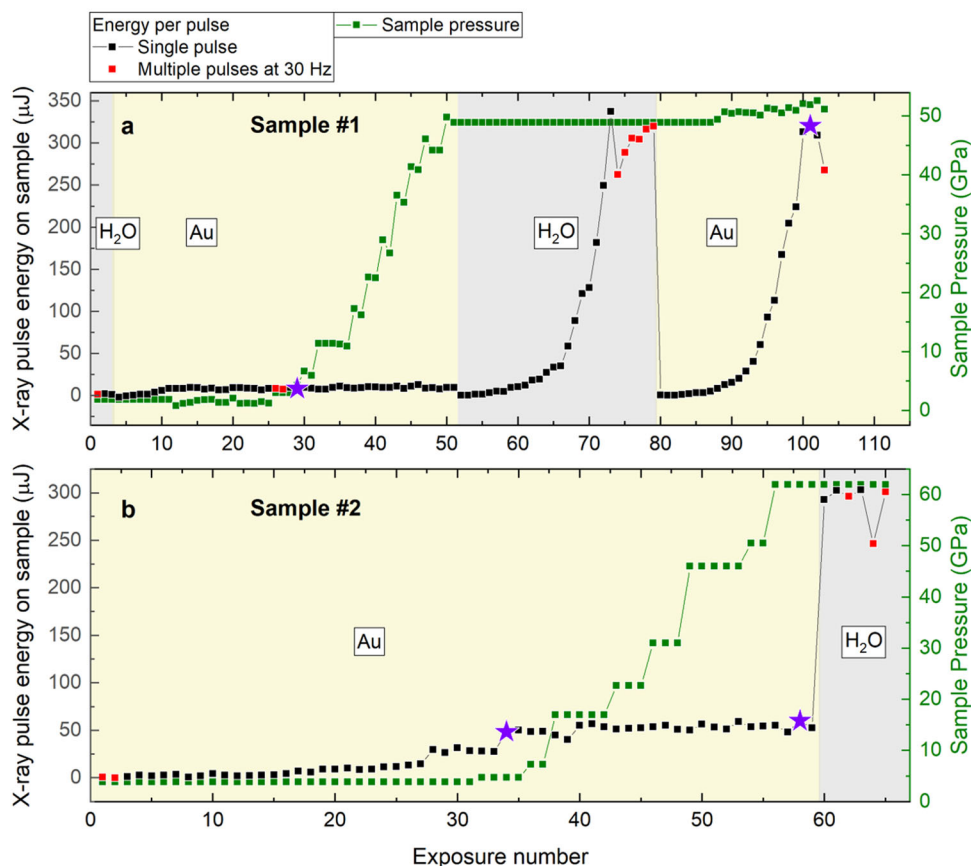


Fig. 3 X-ray exposure history and sample pressure during the PAL-XFEL experiment for samples #1 and #2. The shaded areas indicate whether the X-ray beam was focused on the H₂O (gray) or Au foil (yellow) in (a) sample #1 and (b) sample #2. The X-ray pulse energy incident on the sample is corrected to account for absorption of the upstream diamond anvil. The pressure was determined from the peak position of the (111) Au reflection, as described in the text. For exposures in which the Au reflection was not visible (i.e., when targeting the H₂O), the pressure was assumed to be the same as the previous or subsequent exposure at the same membrane pressure. The purple stars indicate the experimental conditions for which temperature calculations were performed (Supplementary Fig. S10).

of H₂O is heated on timescales of about a microsecond, sufficient for in situ volumetric probing of the H₂O sample state (e.g., by X-ray diffraction), though the repetition rate of the source was not fast enough to capture this excited state. After 33 ms (the time between subsequent pulses) the sample has cooled to the original temperature (Fig. 5), indicating that the spacing between pulses at this facility is too large to perform pump-probe-type heating experiments and that each exposure will probe the cold sample.

According to the heat diffusion model²³, melting tends to be localized to above and immediately adjacent to the Au coupler; this implies the large-scale lateral transport of Au observed in the samples (Fig. 1d) either occurred at very low pressures where the melting temperature of H₂O is low, or that vigorous stirring of the sample by thermo-baric disturbance allowed efficient larger scale (convective) heat transport, which could also drive the multiphase mixing. The improved stabilization of the Au foil and H₂O medium under strong heating observed at higher pressure is attributed to the much faster quenching.

These experiments highlight the possibilities for both pumping and probing samples at high static pressure using XFEL sources. When the X-ray focal size is appropriately chosen (in this case, ~14 μm FWHM used in experiment 1), diamond anvils applying high static pressures are able to mechanically and chemically withstand the effects of high-intensity XFEL pulses over many exposures, even during multiple exposures at 30 Hz, without failure due to radiation damage or the thermal shock created by

fast heating. Assuming a threshold of 0.7 eV for non-radiative diamond damage^{23,28}, the peak energy density in both of our experimental configurations are below the damage threshold, suggesting that diamond damage observed using the small focal size in experiment 2 was most likely caused by the extremely high peak temperature induced by X-ray heating of the Au foil. Our results show that indirect X-ray heating of low-Z materials through the use of a chemically inert high-Z coupler has the potential to access high-temperature phases and conditions at equilibrium that are inaccessible by other techniques.

This strategy for X-ray heating of low-Z and reactive materials to extreme temperatures at high pressure, using an Au absorber, is shown to enable easy access to melting points and even incipient plasma-like states of dense low-Z matter at pressures approaching one million atmospheres, while stabilizing samples via fast heating and quenching. Optical observations, XFEL and synchrotron X-ray diffraction, and secondary electron imaging, suggest that direct X-ray heating of Au during the XFEL experiment resulted in the melting of both Au and the surrounding H₂O, resulting in inter-dispersion of phase-segregated pure fluids at high temperature. In addition, the chemical changes that characterize slower experiments have been eliminated, suggesting a successful cycling of pure water between room and high temperature at high-pressure conditions. Temperature calculations suggest that the samples reached very high peak temperatures (>10,000 K at 4–62 GPa), with local melting of water anticipated even at low X-ray fluences.

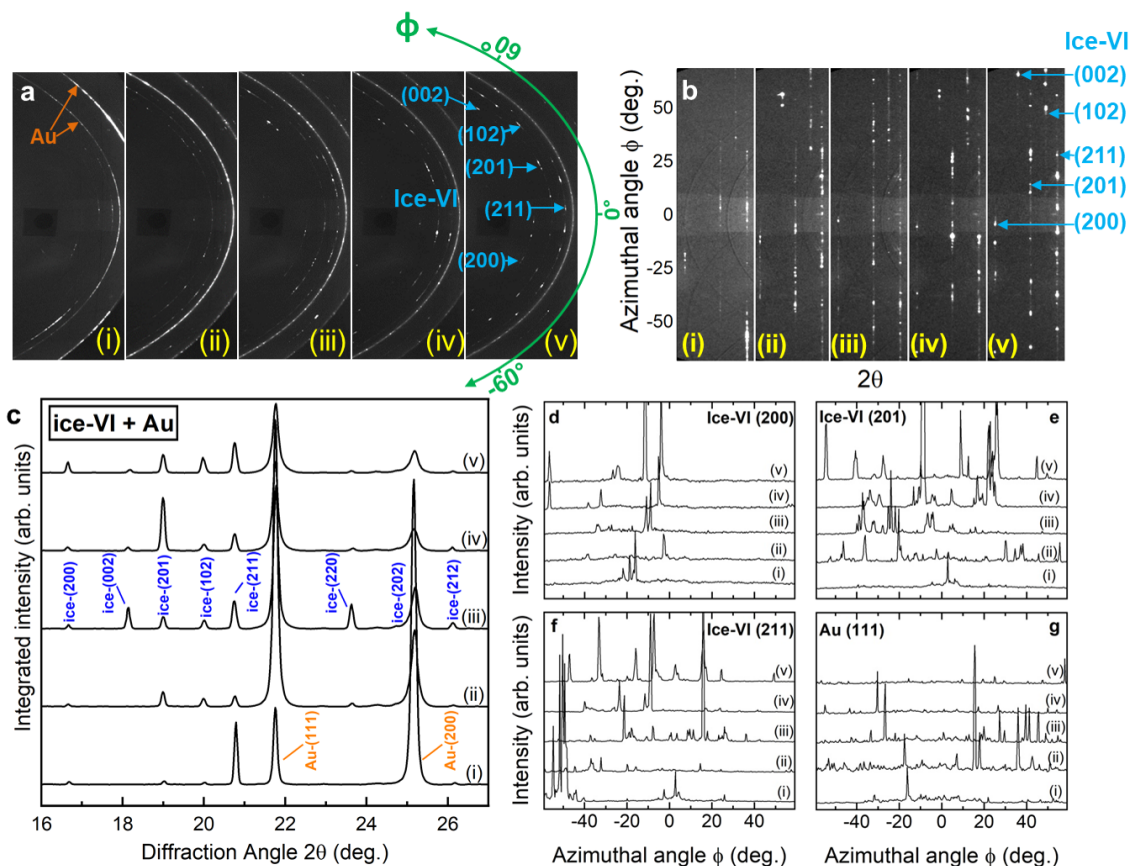


Fig. 4 In situ X-ray diffraction collected at PAL-XFEL during irradiation of sample #3 with 5 X-ray pulses at 30 Hz. The beam was attenuated to 50% of the full X-ray fluence. Diffraction was collected from each individual X-ray pulse, as indicated by labels (i)–(v). The sample pressure was 2 GPa, where H₂O adopts the ice-VI structure. **a** Original and **b** unrolled diffraction images, and **c** integrated diffraction patterns. **d–f** Azimuthal intensity variations of the (200), (201), and (211) ice-VI reflections, respectively. **g** Azimuthal intensity variations for the (111) Au reflection. Significant changes in the azimuthal intensity distribution of both the Au and ice-VI reflections are consistent with melting and recrystallization of the H₂O sample between subsequent X-ray pulses.

The results from these experiments will directly benefit from faster repetition rates of X-ray pulses increasingly available at XFEL facilities, where direct in situ probing of these bulk hot fluid states will be possible. In particular, the 4.5 MHz pulse train of the EuXFEL and complementary pulse-resolved detector capabilities offered by the AGIPD detector will allow for the performance of X-ray pump/X-ray-probe experiments, where subsequent pulses probe the heated state produced by the previous pulse.

Methods

Sample details. For experiment 1, two symmetric piston-cylinder-type DACs were prepared with one c-BN and one WC standard seat and 0.2 mm standard (sample #1) and 0.1/0.3 mm beveled (sample #2) diamonds. For sample #1 (sample #2), a 0.1 mm (0.075 mm) diameter sample chamber was laser-drilled from a pre-compressed 0.025 mm thick Re gasket. After loading, white-light interference measurements between the tips of the diamond anvils determined the initial thickness of the sample chamber to be 13 μm for sample #1 and 15 μm for sample #2, assuming the refractive index of water to be 1.5³⁹. A small piece of 0.002 mm thick Au foil (Goodfellow, Au000070) was placed on the downstream diamond and the sample chamber was filled with Milli-Q water. In both cases, visual observation suggested that the Au foil was insulated from the opposing diamonds by the H₂O ice sample.

For experiment 2, two symmetric piston-cylinder-type DACs were prepared with one standard WC seat and one WC seat of Boehler-Almax design and diamonds with 0.3 mm culets. For sample #3 (sample #4), a 0.13 mm (0.1 mm) diameter hole was drilled in a 0.03 mm thick pre-compressed Re gasket using an electrical discharge machine (EDM). A 0.015 mm thick, 0.2 mm (0.15 mm) diameter step was then EDM'd concentric to the first hole. A strip of 0.002 mm thick, ~0.04 (0.02) mm wide Au foil was placed on the step so that it was not touching the diamond anvils. Ruby powder was sprinkled throughout the sample

chamber to enable pressure measurement, which was then filled with Milli-Q water.

Sample characterization prior to PAL-XFEL experiment. Photomicrographs of the samples were recorded using a Leica M165C stereomicroscope with 120× magnification (Fig. 1a–d and Supplementary Fig. S2). For samples #1 and #2, X-ray diffraction images were collected at the Extreme Conditions Beamline P02.2 (ECB, Liermann2015) at PETRA III (Hamburg, Germany). These data were collected using a 12 keV X-ray beam focused to 16 × 16 μm² (FWHM) using compound reflective lenses (CRL), closely matching the experimental configuration of the PAL-XFEL setup. X-ray diffraction data were collected using a flat panel detector XRD 1621 CT from Perkin Elmer equipped with a ScI scintillator bonded to amorphous silicon readout chip. Sample-to-detector distance (SDD), detector tilt, and detector rotation were calibrated based on the diffraction image from a CeO₂ standard from the National Institute of Standards (NIST 674b) using DIOPTAS⁴⁰.

PAL-XFEL experiment. X-ray diffraction experiments were performed at the XSS station of the PAL-XFEL at Pohang Accelerator Laboratory (PAL) in South Korea²². For experiment 1, the X-ray energy was tuned to 11.998 keV and focused with CRLs to a beam size of 14 × 14 μm² FWHM. For experiment 2, the X-ray energy was tuned to 14,000 eV and focused to 6.5 × 7.5 μm² using Kirkpatrick-Baez (KB) mirrors. In both experiments, the XFEL was operated in the SASE mode. As the X-ray absorption length of Au is very similar at both energies (2.88 μm at 12 keV and 3.14 μm at 14 keV), we expect that X-ray heating is comparable in both experiments, with the main difference being due to focal size. PAL-XFEL provides 25 fs duration X-ray pulses with a maximum fluence of 855 μJ at the sample position (note: this value is not corrected for absorption by the upstream diamond in the DAC). Pulses were provided either as a single pulse, or as multiple pulses at a repetition rate of 30 Hz. The intensity of the pulses was monitored with a Quadruple Beam Position Monitor (QBPM), cross-calibrated to record reliable intensities. The maximum fluency could be significantly reduced by the use of a series of 12 attenuators, which provided as low as 0.3% of the maximum fluency per pulse.

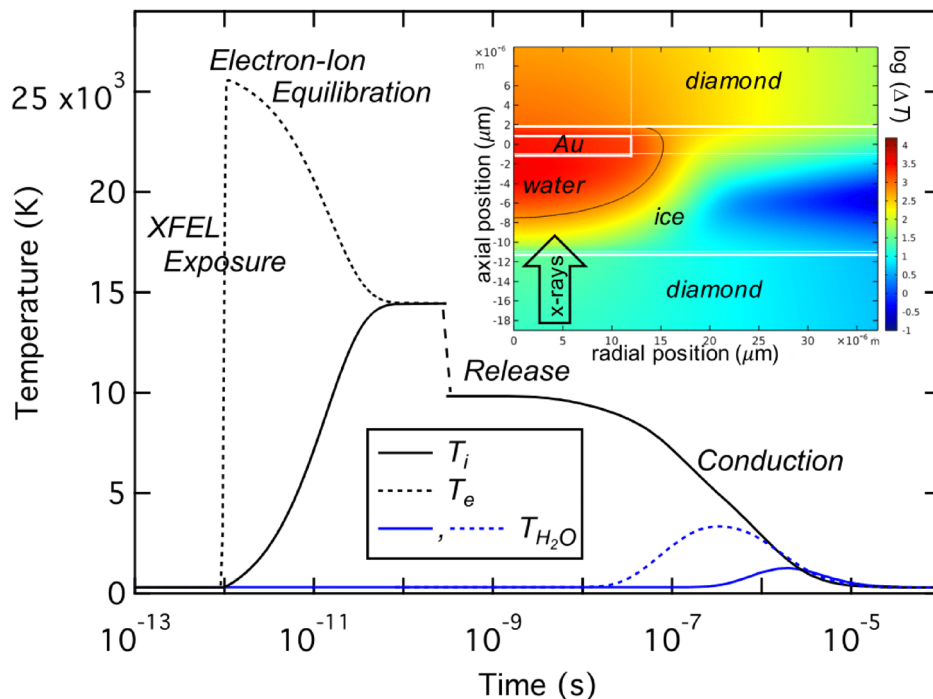


Fig. 5 Calculated temperature-time history of the Au sample. The graph shows the simulated temperature of sample #2 at 4.7 GPa after a 48.6 μ pulse (see Supplementary Table S1), showing sample temperature on the beam axis, at the center of the Au foil (black dotted and solid lines for electron and ion temperature, respectively) and in the water bulk 0.5 and 2 μm upstream from the foil (blue dashed and solid lines, respectively). The XFEL pulse of 25 fs duration strikes the sample at 10⁻¹² s, producing a sharp jump in local electron temperature, which reaches equilibrium with the cold ions on ps timescales³⁷ at constant volume conditions. Following a rapid expansion cooling of the sample, heat conducts out of the sample and into the surrounding cold diamonds at constant pressure²³. The inset shows the temperature distribution and maximum extent of water melting after heating at full power (320 μJ/pulse) on sample #1 at 52 GPa (Supplementary Fig. S10d).

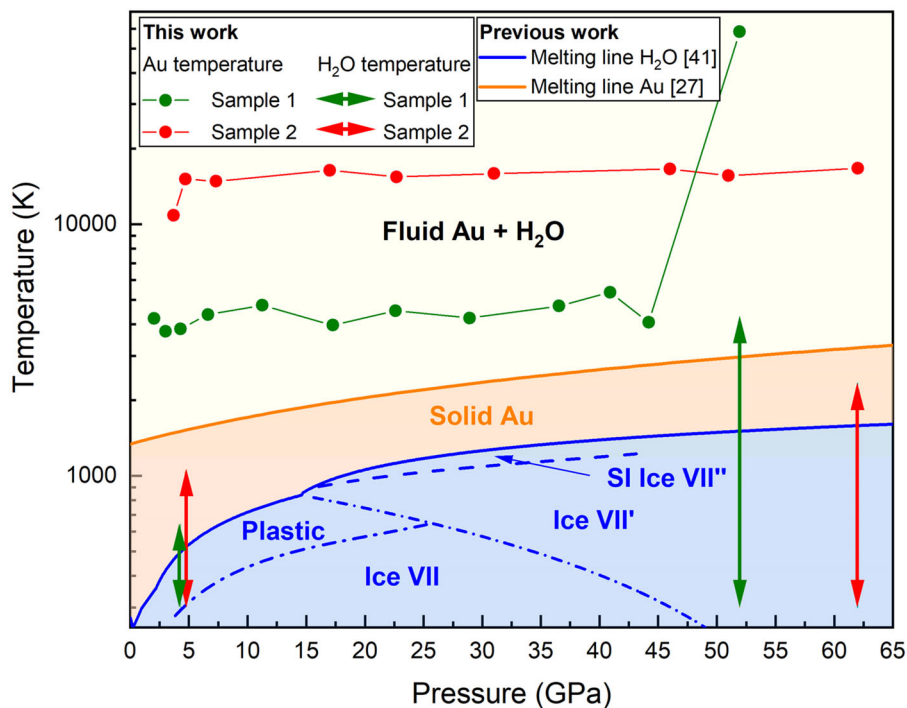


Fig. 6 Phase diagram of H₂O and Au, showing the calculated temperatures determined in samples #1 (green) and #2 (red). The solid circles indicate the peak temperature reached at the center of the Au foil. The arrows show the range of temperatures in H₂O at the time of maximum melting extent following heat conduction for selected pressures (Supplementary Fig. S10), as determined from FEA simulations. The melting lines of Au and H₂O correspond to a Simon-Glatzel fit to the data from Refs. ⁴¹ and ²⁷, respectively; phase lines in H₂O are indicated by broken lines^{41,42}, where SI indicates the superionic phase.

Diffraction images were collected on the Rayonix MX225-HS flat panel detector. SDD, tilt, and rotation of the detector were calibrated with either CeO₂ (experiment 1) or LaB₆ (experiment 2) placed in a DAC aligned to the focus of the optical microscope. When operating with a 30 Hz pulse train, diffraction data were also collected at 30 Hz so that each image corresponded to a single pulse exposure. In this mode, a maximum of 60 images could be collected in a single burst at 30 Hz due to restrictions imposed by the data transfer system. During the experiment, the pressure was controlled remotely through a membrane that was attached to the upstream side of the DAC, inflated through a Pace 5000 pressure controller from General Electric.

When the X-ray focal spot was chosen to be suitably large (~14 × 14 μm²), we found that the diamonds could withstand exposure to full power 12 keV XFEL pulses at pressures up to 62 GPa, despite repeated heating to extreme temperatures, melting, and mass transport.

Post-experimental analysis. Following the XFEL experiments at PAL, post-experimental analysis was performed at the ECB (P02.2). X-ray diffraction maps from samples #1 and #2 were collected using the standard setup (25.6 keV focused to 8 (h) × 3 (v) μm²), and maps from samples #3 and #4 were collected using the KB mirror setup (42.9 keV focused to 2 (h) × 2 (v) μm²). An additional X-ray diffraction map (49 × 49 exposures, 2 μm steps) of sample #2 was collected using the sub-micron focused setup with a 0.8 (h) × 0.8 (v) μm² (FWHM) CRL focused beam at 25.6 keV. Raman scattering maps of samples #1 and #2 were collected using the offline Raman system equipped with an excitation laser wavelength of 532 nm. Secondary electron images of sample #1 were collected at the DESY NanoLab using a SCIOS DualBeam instrument combining a scanning electron microscope (SEM) with a focused ion beam (FIB) from Thermo Fisher (formally FEI) which operates at 5 kV (Stierle2016).

Data availability

The data that support the findings of this study are available from the corresponding author upon reasonable request.

Received: 29 October 2020; Accepted: 29 April 2021;

Published online: 10 June 2021

References

- Hubbard, W. B. Neptune's deep chemistry. *Science* **275**, 1279–1280 (1997).
- Fletcher, L. N. et al. Ice Giant Systems: the scientific potential of orbital missions to Uranus and Neptune. *Planet. Space Sci.* **191**, 105030 (2020).
- Nettelmann, N., Helled, R., Fortney, J. J. & Redmer, R. New indication for a dichotomy in the interior structure of Uranus and Neptune from the application of modified shape and rotation data. *Planet. Space Sci.* **77**, 143–151 (2013).
- Venturini, J. & Helled, R. The formation of mini-Neptunes. *Astrophys. J.* **848**, 95 (2017).
- Cynn, H. C., Boone, S., Koumvakalis, A., Nicol, M. & Stevenson, D. J. Phase diagram for ammonia-water mixtures at high pressures - implications for icy satellites. *Proc. Nineteenth Lunar and Planetary Science Conference*, **19**, 433–441 (Lunar and Planetary Institute, Houston, Texas, 1989).
- Frank, M. R., Fei, Y. & Hu, J. Constraining the equation of state of fluid H₂O to 80 GPa using the melting curve, bulk modulus, and thermal expansivity of Ice VII. *Geochim. Cosmochim. Acta* **68**, 2781–2790 (2004).
- Lin, J.-F. et al. Melting behavior of H₂O at high pressures and temperatures. *Geophys. Res. Lett.* **32**, 11306 (2005).
- Goncharov, A. F. et al. Dynamic ionization of water under extreme conditions. *Phys. Rev. Lett.* **94**, 125508 (2005).
- Sugimura, E. et al. Experimental evidence of superionic conduction in H₂O ice. *J. Chem. Phys.* **137**, 194505 (2012).
- Bezacier, L. et al. Equations of state of ice VI and ice VII at high pressure and high temperature. *J. Chem. Phys.* **141**, 104505 (2014).
- Pruteanu, C. G., Ackland, G. J., Poon, W. C. K. & Loveday, J. S. When immiscible becomes miscible—methane in water at high pressures. *Sci. Adv.* **3**, e1700240 (2017).
- French, M., Desjarlais, M. P. & Redmer, R. Ab initio calculation of thermodynamic potentials and entropies for superionic water. *Phys. Rev. E* **93**, 022140 (2016).
- Bethkenhagen, M. et al. Planetary ices and the linear mixing approximation. *Astrophys. J.* **848**, 67 (2017).
- Malenkov, G. Liquid water and ices: understanding the structure and physical properties. *J. Phys. Condens. Matter* **21**, 283101 (2009).
- Demontis, P., LeSar, R. & Klein, M. L. New high-pressure phases of ice. *Phys. Rev. Lett.* **60**, 2284–2287 (1988).

- Millot, M. et al. Experimental evidence for superionic water ice using shock compression. *Nat. Phys.* **14**, 297–302 (2018).
- Millot, M. et al. Nanosecond X-ray diffraction of shock-compressed superionic water ice. *Nature* **569**, 251–255 (2019).
- Prakapenka, V. B., Holtgrewe, N., Lobanov, S. S. & Goncharov, A. Polymorphism of superionic ice. Preprint at <https://arxiv.org/abs/2007.07715> (2020).
- Dolan, D. H., Knudson, M. D., Hall, C. A. & Deeney, C. A metastable limit for compressed liquid water. *Nat. Phys.* **3**, 339–342 (2007).
- Deemyad, S. & Silvera, I. F. Melting line of hydrogen at high pressures. *Phys. Rev. Lett.* **100**, 155701 (2008).
- McWilliams, R. S., Dalton, D. A., Mahmood, M. F. & Goncharov, A. F. Optical properties of fluid hydrogen at the transition to a conducting state. *Phys. Rev. Lett.* **116**, 255501 (2016).
- Pace, E. J. et al. Intense reactivity in sulfur–hydrogen mixtures at high pressure under X-ray irradiation. *J. Phys. Chem. Lett.* **11**, 1828–1834 (2020).
- Meza-Galvez, J. et al. Thermomechanical response of thickly tamped targets and diamond anvil cells under pulsed hard X-ray irradiation. *J. Appl. Phys.* **127**, 195902 (2020).
- Liermann, H.-P. et al. The extreme conditions beamline P02.2 and the extreme conditions science infrastructure at PETRA III. *J. Synchrotron Radiat.* **22**, 908–924 (2015).
- Nakatsutsumi, M. & Tschentscher, T. *Conceptual Design Report: Scientific Instrument High Energy Density Physics (HED)*. Report no. XFEL.EU TR-2013-003 (PUBDB, 2013).
- Liermann, H. P. et al. *Conceptual Design Report for Diamond Anvil Cell Setup (DAC) at the HED instrument of the European XFEL*. DESY Report, <https://doi.org/10.3204/PUBDB-2021-00846> (PUBDB, 2016).
- Weck, G. et al. Determination of the melting curve of gold up to 110 GPa. *Phys. Rev. B* **101**, 014106 (2020).
- Medvedev, N., Jeschke, H. O. & Ziaja, B. Nonthermal graphitization of diamond induced by a femtosecond X-ray laser pulse. *Phys. Rev. B* **88**, 224304 (2013).
- Schwager, B., Chudinovskikh, L., Gavriluk, A. & Boehler, R. Melting curve of H₂O to 90 GPa measured in a laser-heated diamond cell. *J. Phys. Condens. Matter* **16**, S1177–S1179 (2004).
- Wagner, W., Riethmann, T., Feistel, R. & Harvey, A. H. New equations for the sublimation pressure and melting pressure of H₂O ice Ih. *J. Phys. Chem. Ref. Data* **40**, 043103 (2011).
- Underwood, S. & Mulvaney, P. Effect of the solution refractive index on the color of gold colloids. *Langmuir* **10**, 3427–3430 (1994).
- Mao, W. L. et al. X-ray-induced dissociation of H₂O and formation of an O₂-H₂ alloy at high pressure. *Science* **314**, 636–638 (2006).
- Fukui, H., Hiraoka, N., Hirao, N., Aoki, K. & Akahama, Y. Suppression of X-ray-induced dissociation of H₂O molecules in dense ice under pressure. *Sci. Rep.* **6**, 26641 (2016).
- Cynn, H. et al. Martensitic fcc-to-hcp transformation observed in xenon at high pressure. *Phys. Rev. Lett.* **86**, 4552–4555 (2001).
- Dubrovinsky, L. et al. Noblest of all metals is structurally unstable at high pressure. *Phys. Rev. Lett.* **98**, 045503 (2007).
- Gold, J. S., Bassett, W. A., Weathers, M. S. & Bird, J. M. Melting of diamond. *Science* **225**, 921–922 (1984).
- Mo, M. Z. et al. Heterogeneous to homogeneous melting transition visualized with ultrafast electron diffraction. *Science* **360**, 1451–1455 (2018).
- Lee, K. K. M. et al. Laser-driven shock experiments on precompressed water: Implications for 'icy' giant planets. *J. Chem. Phys.* **125**, 014701 (2006).
- Zha, C.-S., Hemley, R. J., Gramsch, S. A., Mao, H. & Bassett, W. A. Optical study of H₂O ice to 120 GPa: dielectric function, molecular polarizability, and equation of state. *J. Chem. Phys.* **126**, 074506 (2007).
- Prescher, C. & Prakapenka, V. B. DIOPRAS: a program for reduction of two-dimensional X-ray diffraction data and data exploration. *High Press. Res.* **35**, 223–230 (2015).
- Queyroux, J.-A. et al. Melting curve and isostructural solid transition in superionic ice. *Phys. Rev. Lett.* **125**, 195501 (2020).
- Hernandez, J.-A. & Caracas, R. Proton dynamics and the phase diagram of dense water ice. *J. Chem. Phys.* **148**, 214501 (2018).

Acknowledgements

The X-ray experiment was performed at the beamline XSS (proposal no. 2019-1st-XSS-018) at PAL-XFEL funded by the Korean Ministry of Science and ICT (MSIT). Y.L. thanks the support by the Leader Researcher program (NRF-2018R1A3B1052042) of the MSIT. E.J.P. and M.L.M. acknowledge support from EPSRC Grant EP/R02927X/1, and R.S.M. acknowledges support from EPSRC Grant EP/P024513/1. The work by A.L.C. was performed under the auspices of the U.S. Department of Energy by Lawrence Livermore National Laboratory under Contract No. DE-AC52-07NA27344. We acknowledge DESY

(Hamburg, Germany), a member of the Helmholtz Association HGF, for the provision of experimental facilities. Parts of this research were carried out at PETRA-III and DESY NanoLab, and we would like to thank T. Keller, S. Kulkarni and W. Dong for assistance in using the FIB and SEM facilities. V.B.P. was supported by the National Science Foundation – Earth Sciences (EAR-1634415) and Department of Energy-GeoSciences (DE-FG02-94ER14466). Portions of this research were supported through the German Science Foundation DFG Research Unit FOR 2440 (Grant No. MA4534/5-1). We would like to thank B. Ziaja-Motyka and R. Redmer for helpful discussions about the temperature calculations, and C. Prescher for the provision of additional features in the DIOPTAS software. R.J.H. and H.P.L. thank M. Wendt for the preparation of Fig. 2.

Author contributions

R.J.H. prepared the samples and performed the analysis of the diffraction data and the two-temperature modeling. R.J.H., R.S.M., H.P.L., and M.I.M. interpreted the data. S.T. gave advice on the temperature calculations, and R.S.M. performed the FEA calculations. R.J.H., R.S.M., and H.P.L. wrote the manuscript. R.J.H., R.S.M., E.J.P., A.L.C., H.H., J.C., T.K., G.C.H., O.B.B., S.H.C., D.N., S.K., H.C., V.B.P., S.H.S., Y.L., and H.P.L. took part in the experiment.

Funding

Open Access funding enabled and organized by Projekt DEAL.

Competing interests

The authors declare no competing interests.

Additional information

Supplementary information The online version contains supplementary material available at <https://doi.org/10.1038/s43246-021-00158-7>.

Correspondence and requests for materials should be addressed to R.J.H.

Peer review information Primary handling editor: Aldo Isidori.

Reprints and permission information is available at <http://www.nature.com/reprints>

Publisher's note Springer Nature remains neutral with regard to jurisdictional claims in published maps and institutional affiliations.



Open Access This article is licensed under a Creative Commons Attribution 4.0 International License, which permits use, sharing, adaptation, distribution and reproduction in any medium or format, as long as you give appropriate credit to the original author(s) and the source, provide a link to the Creative Commons license, and indicate if changes were made. The images or other third party material in this article are included in the article's Creative Commons license, unless indicated otherwise in a credit line to the material. If material is not included in the article's Creative Commons license and your intended use is not permitted by statutory regulation or exceeds the permitted use, you will need to obtain permission directly from the copyright holder. To view a copy of this license, visit <http://creativecommons.org/licenses/by/4.0/>.

© The Author(s) 2021